

THESIS FOR THE DEGREE OF LICENTIATE OF ENGINEERING

**Heterogeneous deformation of multi-phase  
engineering materials  
- an in-situ neutron diffraction study**

Nitesh Raj Jaladurgam



Department of Physics

CHALMERS UNIVERSITY OF TECHNOLOGY

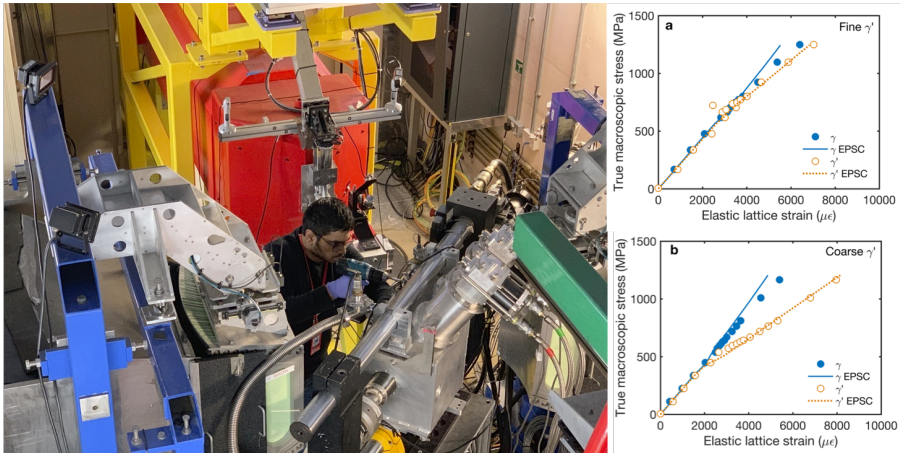
Göteborg, Sweden 2019

Heterogeneous deformation of multi-phase engineering materials  
- an in-situ neutron diffraction study

Nitesh Raj Jaladurgam

© Nitesh Raj Jaladurgam, 2019.

Department of Physics  
Chalmers University of Technology  
SE-412 96 Göteborg  
Sweden  
Telephone + 46 (0)31-772 1000



Cover illustration

The photograph illustrates the tensile loading setup of Engineering diffractometer, Engin-X at ISIS Neutron and Muon source, United Kingdom. The plots indicates the phase specific lattice strains of Haynes 282 when deformed at room temperature shows (a) no significant load transfer between  $\gamma$  and  $\gamma'$  with fine  $\gamma'$  microstructure and (b) definite load transfer from  $\gamma$  to  $\gamma'$  with coarse  $\gamma'$  microstructure.

Printed by Chalmers Reproservice  
Göteborg, Sweden 2019

Heterogeneous deformation of multi-phase engineering materials  
- an in-situ neutron diffraction study  
Nitesh Raj Jaladurgam  
Department of Physics  
Chalmers University of Technology

## Abstract

Gas turbines are complex power generation systems used in aerospace or land-based-power stations. Materials such as Ni-base superalloys are involved in the combustion zone of these machines, which continuously experiences harsh environments with loading at high temperatures. Moreover, the continuous demand for increasing operating temperature to achieve higher efficiencies and reduced emission levels opens the scene to new heat resistant materials like the state-of-the-art high entropy alloys (HEAs), which require a thorough understanding of the structure-process-property relationships. The microstructures of these advanced multi-phase, multi-component alloys are complex, and the deformation is generally heterogeneous both with respect to the different phases and to the crystallographic orientation within each phase. Hence, it is important to understand their behavior and performance during processing and service. In-situ neutron diffraction is a unique technique to probe the deformation behaviour during service/processing-like conditions, including plastic deformation at various temperatures, in order to provide insights into the structure-property relations.

In the first part of this work the deformation mechanisms of a newly developed Ni-base superalloy was investigated using in-situ neutron diffraction and electron microscopy at room temperature. In addition, elasto-plastic self-consistent (EPSC) crystal plasticity simulations are used to obtain insights into the operating deformation mechanisms. In the second part, the as-cast eutectic high entropy alloy AlCoCrFeNi<sub>2,1</sub> was studied using in-situ neutron diffraction at temperatures from 77 to 673 K. These investigations provide unique insights into the complex heterogeneous deformation behavior of these high-performance multi-phase engineering materials.

**Keywords:** Superalloys, Eutectic high entropy alloys, Deformation mechanisms, in-situ Neutron diffraction, Electron microscopy



# Preface

The research work presented in this thesis was carried out at the Division of Materials Microstructure at the Department of Physics, Chalmers University of Technology, during the time period August 2017 - August 2019, under the supervision of Associate Professor Magnus Hörnqvist Colliander and Associate Professor Mattias Thuvander.

This research is funded by the Swedish Foundation for Strategic Research (SSF) within the Swedish national graduate school in neutron scattering, SwedNess. The material was supplied by GKN Aerospace Engine Systems, Trollhättan, Sweden. The authors acknowledge the allocation of beam times (RB1720280, RB1720281 and RB1810499) at ISIS Neutron and Muon Source, Rutherford Appleton Laboratory, United Kingdom.

## List of appended papers

- I. *Microstructure-dependent deformation behaviour of a low  $\gamma'$  volume fraction Ni-base superalloy studied by in-situ neutron diffraction*  
Nitesh Raj Jaladurgam, Hongjia Li, Joe Kelleher, Christer Persson, Axel Steuwer, Magnus Hörnqvist Colliander  
Submitted to Acta Materialia.
- II. *Temperature effects on the load and strain partitioning in AlCoCrFeNi<sub>2.1</sub> eutectic high entropy alloy during tensile deformation*  
Nitesh Raj Jaladurgam, Adrianna Lozinko, Sheng Guo, Tung Lik Lee and Magnus Hörnqvist Colliander  
In Manuscript.

## My contributions to the appended papers

- I. I performed the in-situ neutron diffraction measurements, analysis of results, and wrote the paper.
- II. I performed the in-situ neutron diffraction measurements, analysis of results, and wrote the paper.

# Acknowledgements

It gives me immense pleasure to express my gratitude to the people who have supported me in my first two years of PhD journey. I feel blessed to move to a new country for PhD which allowed me to meet new people and visit new places. First and foremost, I'm greatly thankful to my supervisor Dr. Magnus Hörnqvist Colliander for his continuous support and patience in guiding me through the PhD project. It has been a great experience to sit with you, analyse, discuss the results in different angles and I'm sure it will continue with the rest of my PhD work. My sincere thanks to you for choosing me for this interesting work and supporting me with the necessary guidance. I thank Dr. Mattias Thuvander for being an additional guidance support for my PhD work. I would also like to thank Prof. Christer Persson helping me in the initial days regarding tensile tests at IMS department. I thank GKN Aerospace AB, and Dr. Sheng Guo, Adrianna for supporting me with the tensile samples of Haynes 282 and Eutectic high entropy alloy for my research work.

I am thankful to be part of SwedNess graduate school where I got to meet and participate in courses with enthusiastic PhD colleagues working on wide variety of projects related to neutron scattering. I would like to thank the study director of SwedNess Dr. Martin Månsson for planning and implementing the courses in a very effective way. I am grateful to the staff of Engin-X beamline whose support during beamtimes was invaluable. I extend my gratitude to CMAL staff for training and guidance with electron microscopy and sample preparation work. I would also like to thank Ola Löfgren for his timely help with the Macbook related issues. Also, special thanks to my division members and people from Eva Olsson's group for maintaining such a friendly and positive work atmosphere. I'm grateful to Anand for his help and guidance in the initial days of work with EBSD and other lab activities. Thanks to Masoud, Siamak, Hisham and Anand for making pingpong sessions a fun loaded one. Also, thanks to Jaya Krishna who introduced Body combat to me and a good companion in gym sessions.

I am indebted to my parents for their tremendous support in each step of my life. Lastly, I am grateful to my fiancé, Sneha for her support, patience and unconditional love throughout our long distance relationship. I'm hoping to start a new life with you soon.



---

# Contents

---

<b>1</b>	<b>Introduction</b>	<b>3</b>
1.1	Background . . . . .	3
1.2	Motivation . . . . .	4
1.3	Aim of the study . . . . .	5
<b>2</b>	<b>Deformation mechanisms</b>	<b>7</b>
2.1	Deformation mechanisms of cubic crystal structure . . . . .	7
2.1.1	Face-centered cubic . . . . .	8
2.1.2	Body-centered cubic . . . . .	8
2.1.3	Ordered structure-L1 <sub>2</sub> :Ni <sub>3</sub> (Al,Ti) . . . . .	9
2.2	Deformation of superalloys ( $\gamma$ and $\gamma'$ ) . . . . .	10
2.3	Deformation of High entropy alloys . . . . .	12
2.4	Characterisation methods of deformation mechanisms . . . . .	14
<b>3</b>	<b>Materials</b>	<b>17</b>
3.1	Superalloys . . . . .	17
3.2	High entropy alloys . . . . .	18
3.3	Materials in this work . . . . .	19
3.3.1	Haynes 282 . . . . .	19
3.3.2	Eutectic high entropy alloy . . . . .	20

<b>4</b>	<b>Experimental Methods</b>	<b>21</b>
4.1	Generation of model microstructures . . . . .	21
4.2	Neutron diffraction . . . . .	22
4.2.1	Bragg's law . . . . .	22
4.2.2	Structure factor ( $F_{hkl}$ ) . . . . .	23
4.2.3	in-situ tensile tests using neutron diffraction . . . . .	24
4.2.4	Data analysis methods & tools . . . . .	25
4.2.5	Elasto-plastic self-consistent (EPSC) modelling . . . . .	27
4.3	Electron Microscopy . . . . .	28
4.3.1	Electron channelling contrast imaging (ECCI) . . . . .	28
4.3.2	Electron backscatter diffraction (EBSD) . . . . .	28
4.3.3	Transmission Electron Microscopy (TEM): Image dislocations . . . . .	29
4.3.4	Sample preparation . . . . .	30
<b>5</b>	<b>Results and Outlook</b>	<b>31</b>
5.1	Summary of results . . . . .	31
5.2	Effect of particle size on load partition of low $\gamma'$ volume fraction superalloy at room temperature deformation . . . . .	32
5.3	Effect of deformation temperature on load partition of Eutectic high entropy alloy (EHEA) . . . . .	33
5.4	Outlook . . . . .	34
	<b>Bibliography</b>	<b>35</b>



# CHAPTER 1

---

## Introduction

---

### 1.1 Background

The power generation and aviation sectors are always in search of high performance materials to increase their current capability. Gas turbine engines are the fundamental part of land-based power generation and aircraft propulsion systems. In general, gas turbines has three main components air compressor, combustor and power turbine. In this, the atmospheric air is compressed and feeds it at high pressure into the combustion chamber to ignite fuel with high intensity. This operation generates enormous amount of energy to propel the turbine setup in an aircraft and power generator. Hence, it is crucial to choose eligible materials to build components of gas turbines without any scope for failures. During early days of gas turbines, there were limited materials with high temperature-strength capabilities and stainless steels were used for building components of gas turbines. Due to limited working temperatures and creep-resistance after 540 °C, stainless steels were vulnerable, which motivated to develop Iron, Nickel and Cobalt based superalloys in 1950's [1]. Ni-based superalloys were found to be promising for gas turbines and had about 10 % contribution during 1950's which rose to 50 % by 1985 [2]. This rapid increase of usage was due to development of many superalloys by altering complex chemical compositions followed by design oriented forming and

tailored heat treatments for specific properties. Today, Ni-base superalloys are being used for both rotating and stationary components. Single crystal, directionally solidified and other high  $\gamma'$  volume fraction superalloys are used for rotating parts. Stationary parts are usually made from low volume fraction  $\gamma'$  superalloys such as IN 718 ( $\gamma''$ ,  $\gamma'$ ). IN 718 have an excellent weldability and ideally used in the complex welded assemblies of the gas turbines. However, IN 718 tend to undergo phase transformation from  $\gamma'$  to  $\delta$ , which reduces the high temperature strength over 650 °C. Hence, there is a need to develop weldable superalloy which can work at higher temperatures.

Besides gas turbine engines, many other fields are always in need of new and better materials than conventional materials. These ever growing requirements has been the motivation for the extensive research in the fields of high temperature alloys such as superalloys, stainless steels and so on whose chemistry is designed based on one principal element. Recently, a new class of materials based on multiprincipal-element alloys widely called as High entropy alloys are introduced. These alloys preferably composed of five or more principle elements with equiatomic or near equiatomic ratios (between 5 % and 35 %) and tends to increase the configurational entropy [3]. This phenomena would stabilize these materials to perform better at high temperatures [4]. Many research groups across the globe has been studying these alloys for future potential applications.

## 1.2 Motivation

Superalloys are the traditional class of materials for the application in hot sections of the turbine engines. In the early stages,  $\gamma'$ -strengthened superalloys with volume fraction 25-44 % such as Waspaloy, R-41 and 263 alloys were competent to withstand elevated temperatures. In order to increase the operating temperature there by efficiency, superalloys with better weldability and high temperature resistance are needed. In this context, a new low  $\gamma'$  volume fraction superalloy, Haynes 282 was developed by Haynes International [5] with unique combination of creep strength, fabricability and thermal stability [6]. The size and distribution of  $\gamma'$  particles governs the strength and high temperature capabilities of superalloys. The chemistry of  $\gamma'$  forming elements, Al and Ti was optimised to strike a balance between strength and fabricability [7]. There has been many studies on Haynes 282 focused on macroscopic mechanical properties including tensile strength [8], creep-rupture [6], fatigue [9] and stress relaxation [10] in association with complementary electron microscopy. It is also important to understand the effects of microstructure on the deformation mechanisms addressing structure-property correlation. The effect of microstructure on the load partition mechanism between matrix and particle phase are unknown for low volume fraction  $\gamma'$  superalloys such as Haynes 282.

This motivated to develop a two uni-modal microstructure examined by tensile loading using in-situ neutron diffraction. Also, elasto-plastic self consistent (EPSC) crystal plasticity model was used to predict the evolution of lattice strains to have further insights on deformation mechanisms.

Another class of materials in this work are High entropy alloys. These alloys are in limelight since 2004 through reported literature from Brian Cantor et al. [11] and Yeh et al. [4]. Many High entropy alloys are being designed based on thermodynamic calculations using the CALPHAD (calculation of phase diagrams) method [12]. Earlier, these alloys are tends to form single phase, which couldn't ideally qualify for high performance applications mostly due to trade off between strength and ductility. Li et al. [13] developed a transformation induced plasticity assisted dual phase HEA with fcc and hcp phases to achieve an excellent combination strength-ductility. He et al. [14, 15] had reported the improvement in tensile properties of HEAs through precipitation hardening followed by microstructure control using thermomechanical processing. In the similar lines, eutectic high entropy alloys (EHEA) are introduced by Lu et al. [16] with high fracture strength and high ductility upto 700 °C in as-cast condition. The eutectic microstructure has lamellae of soft fcc and hard bcc phases in AlCoCrFeNi<sub>2,1</sub>. Hence, these alloys are promising for high performance applications in future. The two phase EHEA has been studied using synchrotron diffraction and produced valuable deformation behaviour of fcc phase only [17]. There were no remarks from bcc phase, which tends to be responsible for high strength. This missing puzzle about bcc phase has motivated this work to use in-situ neutron diffraction coupling with tensile loading at cryogenic to elevated temperatures.

### 1.3 Aim of the study

The main aim of this research is to understand the heterogeneous deformation of Haynes 282 and AlCoCrFeNi<sub>2,1</sub> using in-situ neutron diffraction technique as the main experiment tool. In addition, in-house developed 2S-EPSC model was implemented to aid the understanding of deformation behaviour. Furthermore, diffraction insights are complemented using electron microscopy studies. The following research problems have been addressed in this thesis:

- How does the load sharing behaviour of  $\gamma$  and  $\gamma'$  change with the size of  $\gamma'$  particles at room temperature deformation in low volume fraction  $\gamma'$  superalloys such as Haynes 282?
- How does the load partition mechanism changes with deformation temperature of EHEA with complex lamellae microstructure?



## CHAPTER 2

---

### Deformation mechanisms

---

There are different kinds of deformation mechanisms reported and discussed thoroughly across alloys with different crystal structures by Ashby and Langdon et al. [18, 19]. Among them, dislocation slip is the most common mechanisms observed in cubic materials at room temperature. The materials in this study has cubic crystal structure. Thus, deformation of cubic materials is relevant to discuss in this chapter.

#### **2.1 Deformation mechanisms of cubic crystal structure**

It is necessary to discuss the fundamental plastic deformation of individual phases to comprehensively understand the aggregate deformation mechanisms of materials. Hence, the two materials in this work has face centered cubic,  $L1_2$  and body centered cubic structure, and the individual deformation characteristics are discussed here.

### 2.1.1 Face-centered cubic

Face centered cubic materials have 12 potential slip systems which can participate in the plastic deformation. Dislocation slip is the common deformation mechanism at ambient temperature due to presence of close packed structure. The stress required to move a dislocation is given by Peierls Nabarro stress  $\tau_P$  [20].

$$\tau_P = \frac{2G}{1-\nu} \exp\left(\frac{-2\pi h}{b(1-\nu)}\right) \quad (2.1)$$

Here,  $G$  is the shear modulus,  $\nu$  is the Poisson's ratio,  $h$  is the lattice spacing of glide plane and  $b$  is the Burgers vector. It is easy to move the dislocation in case of a close packed structure with low  $\tau_P$  and accommodate strain during deformation of fcc lattice. In fcc, slip always occurs on the  $\{111\}$  plane in the direction  $\langle 110 \rangle$ . The fault in crystal arrangement leads to rise the energy which is proportional to  $G \cdot b^2$ . To reduce the energy, the dislocation can split into two partial dislocations (Eq. 2.2), provided the sum of the square of partials are smaller than the complete dislocation. The partial dislocations are often called as Shockley partials and separated by stacking faults.

$$\frac{a}{2}[110] \implies \frac{a}{6}[211] + \frac{a}{6}[12\bar{1}] \quad (2.2)$$

### 2.1.2 Body-centered cubic

Unlike fcc, Body-centered cubic materials do not have closed packed planes but it has close packed directions. The slip activity usually occurs on closed packed direction  $\langle 111 \rangle$  associated with the planes  $\{110\}$ ,  $\{112\}$  and  $\{123\}$  in the descending order. bcc metals have strong dependency on temperature and strain rate which can effect flow stress at cryogenic to elevated temperatures [21]. It is observed that the screw dislocation motion is the rate controlling mechanism at low temperatures [22], whereas high temperature mechanisms is regulated by edge dislocations with low lattice friction and high mobility [23]. There has been no experimental evidence on splitting of screw dislocations which made it hard to identify the specific slip plane involved during deformation. This has been addressed by Kocks [24] using the idea of pencil glide on  $\langle 111 \rangle$  without well defined slip planes. On a comprehensive study on set of bcc metals, it is found that slip almost always occurs on  $\{110\}$  at low temperatures, which transfers to  $\{112\}$  around 100 K [25]. Unlike in fcc metals, where slip always occurs on  $\{111\} \langle 110 \rangle$  (or  $\{100\} \langle 110 \rangle$ ) at elevated temperatures), bcc metals operate multiple competent slip system with

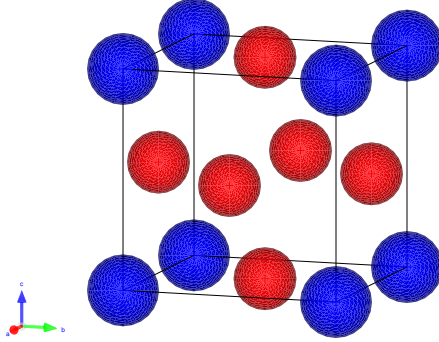


Figure 2.1: L<sub>12</sub> structure with Ni atoms placed at the face centered positions and Al/Ti atoms occupy corners of the unit cell

relative activity depending on the crystal lattice parameter, purity, temperature and mode of loading [25]. In addition, many theoretical models [26, 27] and atomic simulations [28, 29] were implemented in identifying the consistent set of slip planes which can match with experimental observations.

### 2.1.3 Ordered structure-L<sub>12</sub>:Ni<sub>3</sub>(Al,Ti)

The strengthening particle phase  $\gamma'$  in Ni-base superalloys has a simple cubic structure (Pm-3m) and often referred as L<sub>12</sub> type (see Fig.2.1). It has similar potential slip planes of fcc and  $\{111\}$  plane is the active slip from ambient to 700 °C. But the burgers vector has changed from  $a/2 \langle 110 \rangle$  to  $a \langle 110 \rangle$  due to change in the atomic arrangement in the lattice space. As the deformation temperature increases, the slip activity switches from  $\{111\}$  to  $\{100\}$  plane. The transfer of slip activity from octahedral to cube plane is responsible for the rise in the yield strength with deformation temperature leading to anomalous yield strength. This peculiar behaviour prevails between 700-900 °C and depends on the change of the dominant slip plane during deformation [30]. The dislocations in  $\gamma'$  can dissociate similar to matrix phase ( $\gamma$ ) and crucial for change in dominant slip system to show anomalous yield strength. The dissociation of  $\gamma'$  burgers vector is given below.

$$a[\bar{1}01] \longrightarrow \frac{a}{2}[\bar{1}01] + \frac{a}{2}[\bar{1}01] \longrightarrow \frac{a}{6}[\bar{1}\bar{1}2] + \frac{a}{6}[\bar{2}11] + \frac{a}{6}[\bar{2}11] + \frac{a}{6}[\bar{1}\bar{1}2] \quad (2.3)$$

From Eq.2.3, the primary burgers vector dissociates into two partials in a way similar as  $\gamma$  and destroy the ordering by leaving behind an anti phase

boundary (APB). The ordering would be restored by second partial (trailing one) following the leading partial on the same slip plane. Further dissociation of partials leads to Shockley partials by forming a complex stacking fault (CSF) followed by APB (Fig.2.2). Hence, one complete dislocation of  $\text{Ni}_3\text{Al}$  would split into four partial dislocations and often referred as superdislocations.



Figure 2.2: Schematic of dissociation of partials forming superdislocations [31]

## 2.2 Deformation of superalloys ( $\gamma$ and $\gamma'$ )

Superalloys are engineered for high temperature-high stress application and have  $\gamma'$  particles, which act as strengthening agents embedded in  $\gamma$  matrix. The size, volume fraction and distribution of  $\gamma'$  particles have greater impact on the mechanical properties [30].  $\gamma$ ,  $\gamma'$  are coherent phases and undergo plastic deformation on same slip systems. The movement of dislocations occurs usually through glide, climb and cross-slip depending on the deformation temperature and loading conditions. Due to the presence of  $\gamma'$  particles, the plastic deformation occurs mainly in two ways, shearing particles by passing through a pair of dislocations or forming a dislocation loop around these strengthening agents. The occurrence of these mechanisms depends on the size of the particle and volume fraction in  $\gamma$  matrix.

In order to understand these mechanisms, consider the particle shearing condition. It involves two perfect dislocations known as leading and trailing dislocations. The leading one go through the particle and create the anti-phase boundary (APB) and the trailing follows the same glide plane to annihilate the APB. Thus, a pair of dislocations are responsible for plastic deformation

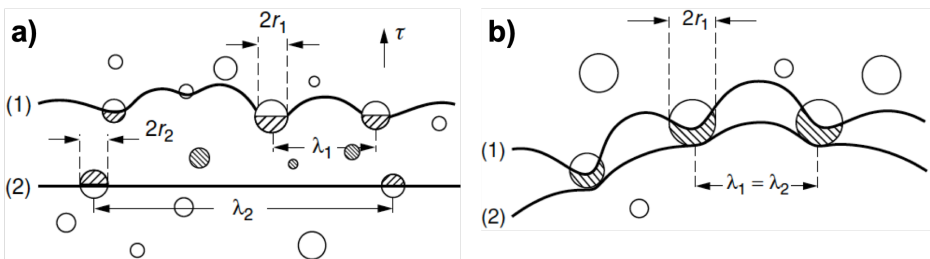


Figure 2.3: Shearing of  $\gamma'$  particles by (a) weakly and (b) strongly coupled dislocations [32]

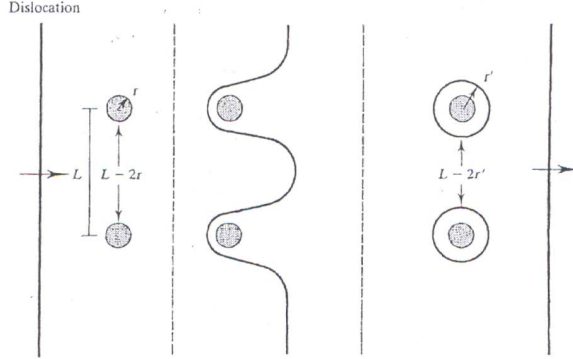


Figure 2.4: The sketch of Orowan process [32]

of  $\gamma$ - $\gamma'$  microstructure. Later, it was observed that the motion of these dislocation pairs depends on the applied shear stress, repulsive force between them and the force associated with APB formation [33, 34]. Furthermore, the relative spacing between dislocation pairs and particle size can have two different shearing phenomena (Fig.2.3). If the particle size is less than the spacing of dislocation pair, it leads to weakly coupled dislocations, otherwise it forms strongly coupled dislocations.

The shear stress to cut through the particles are dependent on the size and volume fraction of the particle for weakly [35] and strongly coupled dislocations [32].

$$\tau_{weak} \propto \gamma_{APB}^{3/2} \sqrt{\frac{rf}{G}} \quad (2.4)$$

$$\tau_{strong} \propto \sqrt{\frac{\gamma_{APB} G f}{r}} \quad (2.5)$$

Here,  $\gamma_{APB}$  is the energy of the anti-phase boundary in  $\gamma'$ ,  $r$  is the radius of the particle,  $f$  is the volume fraction and  $G$  is shear modulus of the particle. In case of weakly coupled dislocations, increasing particle size rises the shear stress but it decreases for strongly coupled dislocations. The rise in volume fraction has the same effect of increasing particle size, since the rise in volume fraction decreases the inter-particle spacing for weakly coupled dislocations. Thus, both volume fraction ( $f$ ) and particle size ( $r$ ) can influence the deformation mechanisms. Moreover, normalized critical resolved shear stress vs. particle diameter (Fig.2.5) has a transition particle size from weak to strong coupling which is ranging from fine to coarse size. Usually, the weakly paired dislocation occurs for under aged condition and strongly paired dislocations are observed in over-aged phenomena. For coarser particles, the strongly coupled shearing mechanism switches to the Orowan process, where the particles are encased by

single dislocations and doesn't cut through particles. Then, the shear stress for Orowan process is given below.

$$\tau_O = \frac{Gb}{L} \quad (2.6)$$

Where  $L$  is the inter-particle spacing. The volume fraction of particles is the another significant parameter from the above three equations. The rise in volume fraction has the same effect of increasing particle size, since the rise in volume fraction decreases the inter-particle spacing. Hence, either volume fraction or particle size can influence the deformation mechanisms.

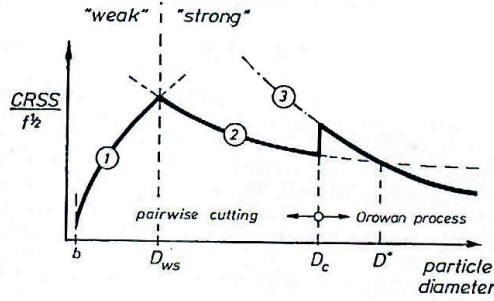


Figure 2.5: The plot shows the normalized critical resolved shear stress with volume fraction vs. particle diameter. Three curves corresponding to weakly, strong coupled dislocation and Orowan process, respectively [32]

## 2.3 Deformation of High entropy alloys

The multi-principle elemental alloys have gained popularity due to their excellent mechanical properties and probables for future potential high temperature applications. These alloys often composed of five or more elements in equiatomic or near equiatomic proportions contributing to high mixing of configurational entropy ( $\Delta S_{mix}$ ) [3]. Thus, these alloys are popularly know as High entropy alloys (HEA) and amalgamation of equiatomic elements to primarily form a single phase cubic structure. The calculation of configurational entropy change per mole for the formation of solid solution from  $n$  number of elements with mole fraction ( $x_i$ ) is given as:

$$\Delta S_{mix} = -R \sum_{i=1}^n X_i \ln X_i \quad (2.7)$$

$R$  is the Universal gas constant (8.314 J/K mol). Alternatively, mixing of equiatomic elements tends to achieve  $\Delta S_{conf} \geq 1.5R$  which became another definition of HEA [3, 36]. Yeh and co-workers [3, 4, 37, 38] had proposed four core effects of HEA which they found to be unique for HEAs: (i) high-entropy

effect- stabilises the solid solution phase formation; (ii) lattice distortion- influences the physical and mechanical properties; (iii) sluggish diffusion- slow kinetics due to cooperative diffusion of different elements; and (iv) cocktail effect- composite effect of mixing different elements. Among four inherent properties, lattice distortion is an important character of HEAs for strengthening solid solution phase. Due to mixing of different elements with atomic size difference tends to huge lattice strain in the unit cell. Moreover, different crystal structure and bond energy of different constituents leads to lattice distortion and atoms occupy non-symmetrical lattice positions unlike in conventional alloys. Hardness and strength of solid solution effectively increases due to the solution hardening in the distorted lattice. Also, the distribution of multiple elements in phases can leads to short range ordering [39], which can control the activation barriers governing defect activities [40]. In addition, cocktail effect believed to effect the composite properties influencing phase formation and stability, physical and mechanical properties, respectively.

Although, the single phase cubic structure can usually possess either high strength or better ductility based on the loading conditions and temperature and the combination of both can be tricky to achieve [41]. Hence, there is a wide scope to develop heterogeneous materials composed of multiple phases to deliver balanced properties. Recently, precipitation strengthened HEAs [14, 42] are introduced with the similar concept of  $\gamma'$  superalloys. However, it demands specific heat treatments to achieve optimum size of precipitates. Hence, Eutectic alloy design which has been studied on steels was extended to HEAs. Liao et al. [43] had proposed the first eutectic multi-phase (fcc and B2) alloy  $\text{Fe}_{30}\text{Ni}_{20}\text{Mn}_{35}\text{Al}_{15}$  in as-cast condition with the combination of good strength and tensile ductility. Later, Lu et al. [16] reported the concept of eutectic high entropy alloy (EHEA) by combining the advantages of eutectic alloys and HEA to have better mechanical properties at elevated temperatures. The tensile deformation of EHEA with composition  $\text{AlCoCrFeNi}_{2.1}$  was reported to have balance of strength and ductility in as-cast condition. Here after  $\text{AlCoCrFeNi}_{2.1}$  is refereed as EHEA in this work. The fine lamellar structure of fcc and bcc phase contributes towards ductility and strength, respectively. The preliminary tensile studies on  $\text{AlCoCrFeNi}_{2.1}$  using in-situ synchrotron diffraction had revealed the orientation specific lattice strain evolution only from fcc and bcc was ignored. Thus, it is significant to have the comprehensive understanding of deformation mechanisms involved in fcc and bcc using in-situ neutron diffraction.

## 2.4 Characterisation methods of deformation mechanisms

Traditionally, Transmission electron microscopy (TEM) is the main technique based on electron diffraction being used to observe the defects and understand deformation mechanisms. The sample volume observed using TEM is limited and may not always qualify to understand the bulk deformation behavior of microstructure. Also, complex in-situ sample holder makes it expensive and usually ex-situ observations are made in TEM. On the other hand, neutron diffraction technique is a unique technique to perform loading tests and simultaneously record series of diffraction patterns to analyse the deformation. Considering the features of neutron such as no charge, large penetration depth would enable to study bulk crystalline samples without any exclusive specimen preparation. The diffraction patterns has peaks whose intensity is relevant to texture, peak broadening interprets the dislocation activity and peak shift gives the lattice strains. There are many large facilities across the globe with neutron reactor and spallation technology facilitating instruments along with many sample environment setups. Essentially, reactor produces constant wavelength neutrons which limits the range of diffraction peak measurements. On the other hand, spallation source implements time of flight approach where neutrons can be tuned to have a range of wavelengths in order to measure diffraction patterns over a wide range using single sample. Currently, there are several spallation neutron source facilities in the world such as ENGIN-X at ISIS neutron and muon source in England, which allows to perform in-situ loading experiments upon beamtime proposal submission.

There has been many studies on superalloys exclusively examined to understand the deformation mechanisms by coupling loading tests with neutron diffraction. Among them, the effect of change in particle size on deformation mechanisms has a great influence on mechanical properties. Daymond et al. had immensely contributed towards the deformation mechanisms with the variation of particle size from ambient to elevated temperatures [44–46]. They studied three uni-modal microstructures of RR1000 at 20 °C, 500 °C and 750 °C, and observed the heterogeneous deformation of  $\gamma$  and  $\gamma'$ . In fine  $\gamma'$ , there was no load sharing between particle and matrix, indicating shearing of particles and confirmed in post-mortem electron microscopy. On the other hand, the load transfer was observed for medium and coarse  $\gamma'$ , indicating the formation of Orowan process. However, these studies are reported on high volume fraction  $\gamma'$  superalloys and low volume fraction  $\gamma'$  superalloys are not studied thoroughly. Hence, it is important to understand the deformation behaviour of low volume fraction  $\gamma'$  superalloys such as Haynes 282 at various loading conditions. Haynes 282 is better than Waspaloy and approaching to R-41 alloy in terms of creep strength and potential candidate for elevated temperature applications [7]. In this study, two uni-modal microstructures of fine (20 nm) and coarse (200 nm) particles are prepared to deform in tensile mode

in conjunction with neutron diffraction. The main goal is to understand the heterogeneous deformation of  $\gamma$  and  $\gamma'$  with difference in particle size at room temperature.

High entropy alloys has been characterised using neutron diffraction. The major analysis was focused on assessing lattice strains in understanding phase transformations [47], lattice distortion [48] and deformation mechanisms [49–51] at different loading conditions. Studies on deformation mechanisms are mostly reported on single phase structures and analysis on dual phase HEAs are limited using in-situ neutron diffraction. In this study, a eutectic high entropy alloy which has a lamellae structure of soft fcc and hard bcc are deformed in tensile mode at 77 K, 300 K and 673 K using in-situ neutron diffraction. These studies are performed to understand the load transfer between fcc and bcc with respect to the deformation temperature.



# CHAPTER 3

---

## Materials

---

### 3.1 Superalloys

Superalloys are an important class of alloys developed for high temperature applications. These alloys are in great demand during World war II due to their exceptional mechanical properties at high temperatures, which are desired for aircraft turbine engines. Creep resistance, fatigue endurance and oxidation resistance has been the critical design criteria for superalloys. Although, these alloys were explicitly designed for gas turbine engines, they are extended to many other fields such as steam turbine power plants, nuclear power systems, chemical industries [2]. In the past few decades, new superalloys with higher operating temperatures are developed to with stand increasing operating temperatures in gas turbines which descended the emission levels.

Superalloys are mainly three categories which are established on the base element with about 11 other alloying elements. They are Nickel-base, Iron-base and Cobalt-base superalloys with common fcc crystal structure, which is preferred for the better combination of strength and toughness at elevated temperatures [30]. Among them, Nickel-base superalloys are popular for aircraft applications due to their resistance to corrosion and better mechanical properties at elevated temperatures.

Superalloys have complex chemistry and derives strength from the formation of various phases in the microstructure. The difference in size of atoms by alloying elements leads to lattice distortion and imparts strength from the solid solutioning effect forming the matrix phase called Gamma ( $\gamma$ ) with fcc crystal structure. Along with base element Ni (for Ni-base superalloy), the other alloying elements such as Mo, Cr, Co, Fe, etc. contributes for solid solution strengthening. Another important mechanisms which enabled superalloys to strengthen at elevated temperature is precipitation strengthening. It involves in formation of precipitates known as  $\gamma'$  or  $\gamma''$  as secondary phase with an ordered structure and maintained lattice coherency with the matrix phase. These precipitates contain Al, Ti and Nb, forming  $\text{Ni}_3(\text{Al,Ti})$  and  $\text{Ni}_3\text{Nb}$  which are  $\gamma'$  and  $\gamma''$  of simple cubic ( $L1_2$ ) and body centered tetragonal ( $D0_{22}$ ), respectively. These precipitates are the main strengthening agents which hinder the dislocation motion at high temperatures and enable abnormal increase in strength over 600 °C due to change in operating slip system from  $\{111\}$  to  $\{100\}$  [30]. Further,  $\delta$  phase with ordered orthorhombic structure is critical for regulating grain size contributing for improvement in creep-rupture strength. Also, the precipitation of MC type carbides are prevalent due to the presence of carbon in traces (0.02 % to 0.2 %) and ageing treatment forms  $\text{M}_6\text{C}$  or  $\text{M}_{23}\text{C}_6$  which prevents the grain boundary sliding and allow stress relaxation. Other miscellaneous but perilous phases such as  $\sigma$ ,  $\mu$  or Laves phases are called Topologically close packed (TCP) phases, which are detrimental and affect the creep-rupture strength and ductility due to their needle-like morphology in the microstructure. TCP phase are usually formed due to solute segregation which are usually eliminated during solution treatment.

### 3.2 High entropy alloys

High entropy alloys are new class of materials based on multi-principle elemental alloys with high mixing configurational entropy. The concept of multi-principle elemental alloys was introduced by two independent research groups, Cantor et al. [11] and Yeh et al. [4] in 2004. They proposed the increase in addition of equiatomic elements can increase the configurational entropy and reduces the free energy of the alloy effecting the stability of solid solution. These alloys are typically composed of at least five elements in equal proportions forming a single phase crystal structure primarily due to configurational entropy [52]. Moreover, non-configurational entropy and enthalpy play a crucial role in phase formation and stability from the thermodynamics view. Hence, the theory of high entropy concept merely justify the formation of phases and is debatable in this field. Apart from the ambiguity about the role of entropy, many studies were reported on HEAs due to unique multi-principle element alloy design with better properties compared to conventional alloys [53]. These alloys are reported to have four distinct characteristics [37].

- High entropy effect- claims to stabilize the phase formation at elevated temperatures
- Lattice distortion effect- difference in atomic sizes, crystal structure and bonding energy leads to influence the properties.
- Sluggish diffusion effect- due to compact and limited atomic sites leads to low lattice potential energy sites and reduces the diffusion kinetics [54].
- Cocktail effect- combined effect of constituents on properties.

### 3.3 Materials in this work

Two newly developed different class of materials which includes the Ni-base superalloy, Haynes 282 and Eutectic high entropy alloy, AlCoCrFeNi<sub>2,1</sub> are studied in this work. The newly developed low  $\gamma'$  volume fraction superalloy Haynes 282 was deformed at room temperature to understand the influence of  $\gamma'$  particle size on the deformation mechanisms. EHEA was investigated to understand the effect of deformation temperature on the heterogeneous deformation of fcc and bcc phases. Both these experimental studies were performed using in-situ neutron diffraction followed by analysis of deformed microstructure using electron microscopy techniques.

#### 3.3.1 Haynes 282

Haynes 282 is a newly developed  $\gamma'$  superalloy by Haynes International [5] for high temperature structural applications in aero and land-based gas turbine engines. Haynes 282 is designed as a low  $\gamma'$  volume fraction superalloy to improve the weldability without losing excellent creep strength in the temperature range of 650 to 900 °C [6]. This alloy has better fabricability compare to the Waspaloy, C-263 and R-41 which are the conventional superalloys in application. Also, thermal stability and ductility around 871 °C was found to be better than R-41 alloy. Haynes 282 also has better oxidation resistance at 927 °C in comparison with other competent alloys. The chemical composition of Haynes 282 can be seen in Table. 3.1. The presence of Cr content provides the resistance to oxidation and hot corrosion, while Co regulates the  $\gamma'$  solvus. Mo content is limited to 8.5 % for excellent creep strength. The critical composition of Al (2.1 %) and Ti (1.5 %) are optimised to improve the weldability while maintaining the desired high temperature creep strength. Other minor additions like B and C are added to improve mechanical properties. The conventional heat treatment for Haynes 282 is 1010 °C/2h/aircooled and

788 °C/8h/aircooled, which forms spherical  $\gamma'$  particles with discrete carbides ( $M_6C$  and  $M_{23}C_6$  type) along the grain boundaries.

Table 3.1: Chemical composition of Haynes 282 by wt. %

Cr	Co	Mo	Ti	Al	Fe	B	P	S	Si	Ni
19.52	10.33	8.56	2.13	1.52	0.66	0.005	0.002	0.002	0.6	Bal

### 3.3.2 Eutectic high entropy alloy

The concept of eutectic high entropy alloy (EHEA) was proposed by Lu et al. [16] by combining the principles of eutectic alloy and high entropy alloy. This strategic design approach had led to achieve a lamellar microstructure of soft fcc and hard bcc phases. The complex microstructure was reported to have a remarkable combination of high tensile ductility and high fracture strength from 77 K to 973 K in as-cast condition. The chemical formulae of EHEA is  $AlCoCrFeNi_{2.1}$  and the detailed chemistry can be seen in Table.3.2.

Table 3.2: Chemical composition of EHEA by at. %

Al	Co	Cr	Fe	Ni
17.88	16.24	16.16	16.08	33.64

The literature has reported a detailed microstructure characterisation of EHEA and confirmed the presence of Ni,Al rich B2 phase and Fe,Co,Cr rich  $L1_2$  phase [55]. Gao et al.[56] reported Cr-rich nano precipitates in B2 phase and Zhang et al. [57] supported the formation of precipitates in both  $L1_2$  and B2 phases. Furthermore, other groups had implemented thermo-mechanical treatments followed by annealing to achieve better mechanical properties compare to as-cast condition. Wani et al. [58] had performed cryo-rolling and annealing (800 °C) led to ultra fine lamellar structure of fcc and bcc. This heterogeneous microstructure had achieved UTS  $\sim$  1.2 GPa with elongation to failure  $\sim$  14 %. Later, Battacharjee et al. [59] had reported the yield stress of 1437 MPa, UTS of 1560 MPa with elongation till 14 % by different cryo-rolling approach. Other groups [60–62] had designed and implemented complex cryo-rolling and annealing treatments to accomplish improvements in high strength and high ductility.

# CHAPTER 4

---

## Experimental Methods

---

There are two main experimental techniques involved in this work, namely neutron diffraction and electron microscopy. These techniques are discussed including sample preparations in detail in this chapter.

### 4.1 Generation of model microstructures

The superalloy, Haynes 282 was provided by GKN Aerospace AB. The alloy was produced via casting, followed by forging and the initial composition is shown in Table.3.1. Later, the forged bars were machined to obtain cylindrical samples suitable for tensile tests. These samples were subjected to two types of heat treatments to achieve fine and coarse  $\gamma'$  particles, respectively. In case of fine  $\gamma'$ , the samples were homogenized at 1120 °C and water quenched to annihilate the signs from forging. Later, it was heated to 1010 °C for carbide stabilisation and air cooled to room temperature. The final step was focused on ageing, involving nucleation of fine  $\gamma'$  particles at 788 °C for 8 hours followed by air cooling. For coarse  $\gamma'$ , the heat treatments were continuous without intermittent cooling steps. It has started with homogenization at 1120 °C followed by control cooling rate at 10 °C/min to 950 °C, held for half an hour and continued to slow cooling at 0.1 °C until 500 °C followed by water quench.

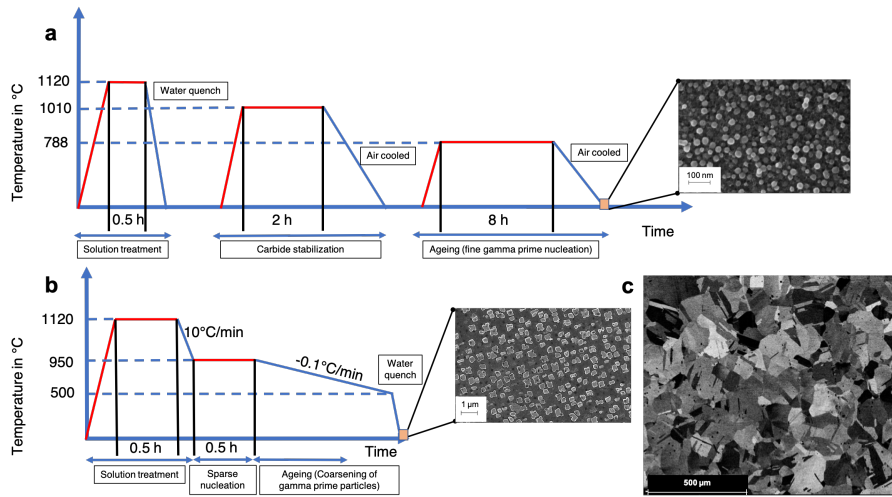


Figure 4.1: Heat treatments on Haynes 282 to obtain (a) Fine  $\gamma'$ , (b) Coarse  $\gamma'$  and (c) Overview of coarse grains with annealing twins.

Using these heat treatments, fine  $\gamma'$  has about 20 nm and coarse one has 200 nm with 20 % volume fraction each in  $\gamma$  matrix.

## 4.2 Neutron diffraction

Diffraction is one of the powerful research tools in the field of materials science used to probe crystalline materials. It is generally used for identification of phases, orientation distributions, crystal defects and works on elastic scattering based on the Bragg's law.

### 4.2.1 Bragg's law

Diffraction occurs only through coherent elastic scattering from atoms arranged in crystal planes having d-spacing at well-defined scattering angles. From Fig.4.2, a couple of elastic scattering events are shown on successive planes with d-spacing ' $d$ ' (nm), incident and diffracted wave vectors,  $k_i$  and  $k_f$ , respectively. The incident wave scatters and diffracts at an angle  $\theta$  and total diffraction angle is  $2\theta$ . The two scattered waves would travel distances differ by  $2d\sin\theta$ , and may out of phase with each other. Nonetheless, if the the extra distance for scattering from the successive lattice planes is equal to a whole integral number,  $n$ , of wavelength  $n\lambda$ , then the scattered waves will be

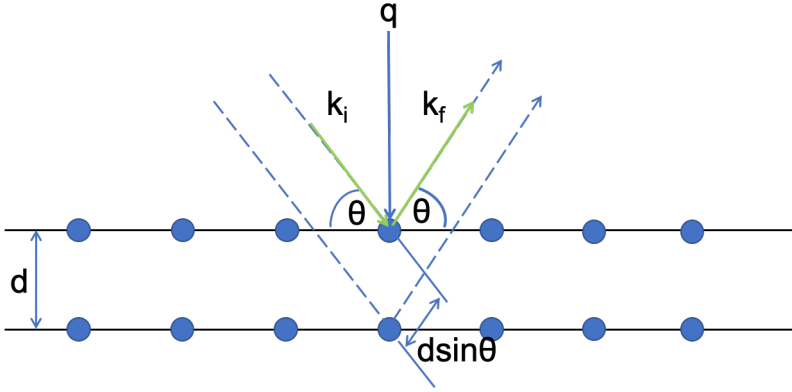


Figure 4.2: Coherent scattering events on a pair of atomic planes

in phase and the total scattered amplitude will be added from each scattering event [63]. The Bragg condition is expressed as given below.

$$n\lambda = 2d \sin \theta \quad (4.1)$$

Also, the scattering event can be expressed using resultant scattering vector ( $q$ ), incident ( $k_i$ ) and diffracted wave vectors ( $k_f$ ), respectively.

$$q = k_i - k_f = 2\pi/d \quad (4.2)$$

X-rays, neutrons and electrons are three popular sources of radiation used in diffraction experiments to probe the crystalline materials at different length scales. Electrons and X-rays are scattered by the electron clouds of the atoms in lattice space. These are ideal for surface studies involving depth from nm to few  $\mu\text{m}$ . Later, synchrotrons are introduced, which are high energy X-ray sources capable of probing few cm with high brilliance. On the other hand, neutrons have high penetration and doesn't have charge associated with them, in contrast to X-rays and electrons. Neutron diffraction delivers similar crystallographic information as X-rays by accounting larger gauge volume  $\approx (1000 \text{ mm}^3)$ . The combination of probing large gauge volume, high penetration depth and no charge features has made the neutron diffraction as a unique technique to assess the bulk response of the material in this study.

## 4.2.2 Structure factor ( $F_{hkl}$ )

Structure factor is the measure of amplitude and phase of a wave diffracted from the crystal planes defined by Miller indices ( $h,k,l$ ). The mathematical

equation of structure factor is given below.

$$F_{hkl} = \sum_i f_i \exp 2\pi i(hx_i + ky_i + lz_i) \quad (4.3)$$

Here, the sum indicates the over all atoms in the unit cell having  $x_i, y_i, z_i$  positional coordinates of  $i^{th}$  atom.  $f_i$  is the scattering length density of  $i^{th}$  atom of the respective phase Miller indices  $(h, k, l)$ . It is important to observe  $f$ , whose value changes with the type of atom and source of radiation. For X-rays,  $f$  depends on the interaction of outermost electrons of an atom and follows a specific trend with increase in atomic number. However, neutron source interact with nucleus of an atom and doesn't have any trends of  $f$  unlike X-rays. Also, the intensity of a diffracted beam is directly related to the amplitude of structure factor, whose values depends on the  $f$  and  $(h, k, l)$  Miller indices. Hence, it is possible to get zero intensity if  $f$  is zero despite  $(h, k, l)$  plane has diffracted. For instance,  $\gamma'$  superlattice peaks are not detected by X-rays due to zero scattering length density of  $\text{Ni}_3(\text{Al}, \text{Ti})$ . On the other hand, neutrons scattering length of Al and Ni are positive and Ti is negative and the resultant is not zero, which made it possible to capture  $\gamma'$  superlattice peaks.

### 4.2.3 in-situ tensile tests using neutron diffraction

The large scale facilities involving generation of neutrons for scattering (diffraction) experiments have also built sample environment set-ups to enable in-situ measurements. In this study, in-situ tensile loading was combined with neutron diffraction to measure the lattice strain evolution during deformation. The in-situ loading tests can provide insights on the micromechanics of polycrystalline materials. In case of multi-phase materials, phase specific elastic strains can be extracted from the respective diffraction pattern of each phase. Analysing all phase elastic strain attributes to the bulk deformation behavior of the material. In this work, the cylindrical tensile test specimens of 6 mm diameter with 25 mm gauge length were used for in-situ tensile tests. The experiments were performed at Engin-X beamline at ISIS pulsed neutron source, Rutherford Appleton Laboratory, United Kingdom [64]. The stress rig was located at  $45^\circ$  to the incident beam direction and two detectors were placed to measure the lattice strains both parallel and perpendicular to the loading axis simultaneously as shown in Fig.4.3.

For Haynes 282, the two uni-modal microstructures were used and tensile tests were performed at room temperature to study the effect of particle size on deformation mechanisms. For EHEA, the lattice strains were measured at 77 K, 300 K (room temperature) and 673 K, respectively to study the effect of temperature on deformation mechanisms. In both the cases, the gauge volume in the beam is  $4 \times 4 \times 4 \text{ mm}^3$ . Despite the fact that neutron diffraction have

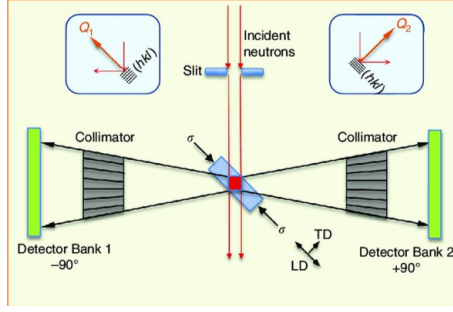


Figure 4.3: Schematic of Engin-X instrument at ISIS Neutron and Muon source, UK [65]

large penetration depth, they also have weaker interaction, low flux and needs longer time to deliver optimum (reasonable) signal to noise particularly in case of superalloy involving superlattice reflections  $\gamma'$ . Hence, the monotonous loading tests are not feasible, instead the samples are loaded under position and load control monitored by extensometer and load cell. The respective diffraction patterns are captured while holding the sample in position and load control during the tensile test.

#### 4.2.4 Data analysis methods & tools

The engineering diffractometer Engin-X is used for in-situ neutron diffraction experiments in this work. Engin-X is a time of flight (TOF) neutron strain scanner, where a pulsed beam of neutrons with wide range of energy scatters the sample and detected at a fixed  $2\theta$  and the wavelength ( $\lambda$ ) of the detected neutrons are defined in terms of TOF,  $t$  as follows

$$\lambda = \frac{h}{m(L_1 + L_2)}t \quad (4.4)$$

Where  $h$  is the Planck's constant,  $m$  is the neutron mass and  $L_1$  and  $L_2$  are primary and secondary flight paths, respectively. The measured diffraction patterns has  $(hkl)$  lattice planes corresponding to family of grains in the bulk sample. The recorded TOF from the detectors can be converted to d-spacing using the following relation.

$$d_{hkl} = \frac{h}{2 \sin \theta_B m(L_1 + L_2)}t_{hkl} \quad (4.5)$$

In this study, the single peak fit is the main analysis method used to identify the peak centre ( $d$ ), peak width (Full width half maxima) and peak integrated intensity. These three measured entities carry the information on

lattice strain, defect density and texture of the respective ( $hkl$ ) planes. In this study, GSAS-II software [66] has been used to perform single peak fit analysis for the measured diffraction patterns of Haynes 282 and EHEA.

## Visualisation of neutron diffraction results

The neutron diffraction gives the diffraction patterns containing orientation specific peaks corresponding to the phases present in the crystalline material. During in-situ loading tests, the peak shifts would occur which corresponds to lattice strains measured along specific orientation. The lattice strains are calculated using Eq.4.6.

$$\epsilon = \frac{d_{hkl} - d_0}{d_0} \quad (4.6)$$

Here,  $d_{hkl}$  and  $d_0$  are d-spacing values at any given instant load and no load conditions, respectively. It has been a regular practice in the literature to plot macroscopic stress against phase and orientation specific strains to observe the distinct load sharing phenomena between phases and respective orientations. For example, Haynes 282 with coarse  $\gamma'$  microstructure showing the load transfer between matrix ( $\gamma$ ) and particle phase ( $\gamma'$ ) is evident from Fig.4.4(a). Similarly, the plastic anisotropy of fundamental planes can be observed in Fig.4.4(b).

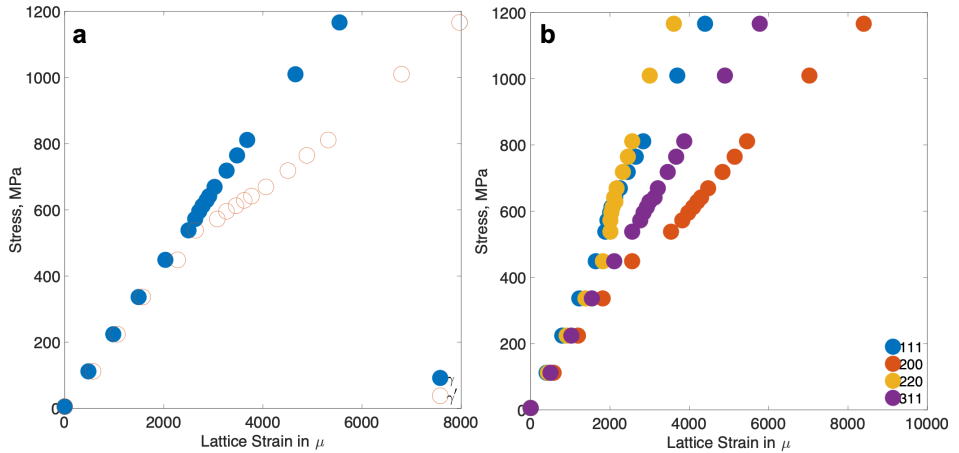


Figure 4.4: (a) Phase specific stress-strain and (b) Orientation specific stress-strain plots

However, the phase and orientation specific stresses can be calculated from

the measured lattice strains using Hooke's law (Eq.4.7).

$$\sigma = E_{phase/hkl} \times \epsilon_{phase/hkl} \quad (4.7)$$

$E_{phase/hkl}$  is the Young's modulus of phase or  $\{hkl\}$  plane,  $\epsilon_{phase/hkl}$  is the lattice strain of phase or  $\{hkl\}$  plane. Typically, the plot of phase and orientation specific stress vs. lattice strains will lead to a linearity with overlaps and doesn't distinctly indicate the load partition between phases and respective orientations. In this work, load partition between phases is an important aspect to observe with varying microstructures and deformation temperatures. Thus, the lattice strains are plotted against macroscopic stress to understand the load transfer between phases.

#### 4.2.5 Elasto-plastic self-consistent (EPSC) modelling

The deformation behaviour of any hkl reflections doesn't solely depends on the Schmid factor and elastic constant, rather depends on the constraints from the surrounding grains. In order to understand the complex deformation behaviour of polycrystals, several models were proposed and practised. Among them, self consistent (SC) models are popular in aggregate deformation response with less computational efforts.

Firstly, SC models were developed based on the Hill SC approach [67] and implemented by Hutchinson [68]. It assumes that each grain is an ellipsoidal inclusion in Homogeneous Equivalent Medium (HEM) which represents the average properties of polycrystals. Initial studies were focused on residual stresses of single phase materials [69]. There are many studies based on single phase materials and later a large strain visco-plastic self consistent (VPSC) model was developed and implemented on Ti alloys [70]. This model accounts for co-rotation of grains, which share the slip systems during plastic deformation. However, VPSC doesn't give information about elastic lattice strains which is required to compare with neutron diffraction results. Later, a 2-site elasto-plastic self consistent (2S-EPSC) model was proposed by Dye et al. [71] and Daymond et al. improved the model to exclusively predict the lattice strain evolution of  $\gamma'$  strengthened Ni-base superalloys at different deformation temperatures [45, 46]. Although, the model is in good agreement with the experimental lattice strain evolution, it doesn't implement co-rotation phenomenon between  $\gamma$  and  $\gamma'$  and the texture development is unknown due to small strain formulation. Recently, Li et al. [72] had developed and implemented a 2-site EPSC model which particularly accounts for co-deformation of phases along with crystallographic texture developments under finite strain applications. Extended Voce laws [73, 74] were used to describe the plastic deformation of the grains. This model is coupled with in-situ neutron diffraction studies of Haynes 282 under this study. A set of 5000 randomly oriented

grains (the random texture of the starting material was confirmed experimentally), generated from a uniform orientation distribution, was used as starting condition. Both global and lattice specific stress-strain curves were used to fit the model.

## 4.3 Electron Microscopy

The deformed samples are sectioned and prepared to observe the deformed microstructures using Scanning electron microscope and Transmission electron microscopes.

### 4.3.1 Electron channelling contrast imaging (ECCI)

The ECCI is a mode of imaging in SEM involving channelling effect of electrons through a crystalline materials and images with crystallographic orientation contrast. The electrons travel parallel to planes of crystalline material without intense interaction and leads to electron channelling with minimum back scattering signal. If the crystals are imperfect with defects such as dislocations and stacking faults then the electron beam interacts with inclined plane and emits strong back scattered signals due to Bragg diffraction from the position of defects. The imaging with these mechanisms form a dark and bright features in the microstructure replicating normal crystal lattice and defects, respectively.

The following requirements are usually practised to get the optimum electron channelling contrast [75].

- Beam must be parallel and collimated by choosing appropriate aperture size.
- High beam current is maintained during analysis to get optimum back scattered signal
- Spatial resolution directly depends on the beam diameter and electron channelling prefers broad beam diameter to receive sufficient signal for imaging.

### 4.3.2 Electron backscatter diffraction (EBSD)

EBSD is an ideal technique to measure the crystallographic orientations in bulk at the surface level in crystalline materials. The set-up includes tilting

stage to  $70^\circ$  with respect to the normal plane of incident beam and back scattered electrons are generated on interaction with the inclined sample. The back scattered signals are detected as kikuchi lines representing crystal planes recorded on phosphorus screen (detector) [76]. The recorded Kikuchi patterns are visualised in different ways based on the type of analysis. In general, the presence of texture is visualised using inverse polefigures (IPF) maps. The IPF maps follow a specific color scheme to represent different orientations measured from the microstructure. Alternatively, local misorientation maps are appropriate to look at defect structures. Kernel Average misorientation (KAM), Grain reference orientation deviation (GROD) and Grain orientation spread (GOS) are the ways to represent the misorientations from the deformed microstructure [77]. KAM is based on the misorientation between the point of interest (POI) and definite set of points around POI. GROD measures the misorientation between a point and mean orientation of the grain. GOS is the average misorientation between a point and mean orientation of the grain. In this study, GROD in combination with KAM are used to interpret the critical features of deformed microstructure of Haynes 282.

### 4.3.3 Transmission Electron Microscopy (TEM): Image dislocations

TEM is an unique tool to observe features of microstructure at micron to nano scale with good resolution. TEM is used to study dislocation in this work. In order to observe dislocations, one need to follow  $\mathbf{g} \cdot \mathbf{b}$  rule. Here,  $\mathbf{g}$  corresponds to the diffraction vector (indeed a plane) and  $\mathbf{b}$  represents the burgers vector of the crystal system. The sample is tilted with respect to the incident electron beam to alter  $\mathbf{b}$  with respect to  $\mathbf{g}$  and obtain perfect diffraction conditions to observe dislocations. If  $\mathbf{g} \cdot \mathbf{b} = 0$ , diffraction contrast will be minimum and one cannot resolve the line defects. On the other hand if  $\mathbf{g} \cdot \mathbf{b} \neq 0$ , then these defects can be observed with good diffraction contrast in TEM. To do this analysis, the possible burgers vectors,  $\mathbf{b}$  and diffraction vector,  $\mathbf{g}$ , should be known for given crystal system which satisfies  $\mathbf{g} \cdot \mathbf{b} \neq 0$ . Table. 4.1 helps in choosing relevant diffraction plane for imaging dislocations [78].

The dot product of  $\mathbf{g}$  and  $\mathbf{b}$  were evaluated at each combination and the result is tabulated. According to  $\mathbf{g} \cdot \mathbf{b}$  rule, the highlighted yellow colored rows satisfy the  $\mathbf{g} \cdot \mathbf{b}$  rule to observe dislocations. Hence, either  $(\bar{1}\bar{1}1)$  or  $(200)$  or both can be chosen to observe and study dislocations. These diffraction vectors exists in specific zone axis,  $(200)$  and  $(\bar{1}\bar{1}1)$  can be observed in  $[011]$ . Hence, one should obtain  $[011]$  zone axis using double tilt holder which rotates perpendicular to X and Y directions. Selected area diffraction aperture is used to select the two beam condition at  $(200)$  and the corresponding the bright field image is captured with the help of objective aperture.

Table 4.1: The burgers vectors and diffraction planes of FCC are tabulated as per  $\mathbf{g} \cdot \mathbf{b}$  rule. Yellow coloured row gives the selected  $\mathbf{g}$  and  $\mathbf{b}$  combinations to resolve dislocations [78].

$\mathbf{g} \backslash \mathbf{b}$	$\frac{1}{6}[\overline{112}]$	$\frac{1}{6}[\overline{1\bar{2}1}]$	$\frac{1}{6}[\overline{211}]$	$\frac{1}{3}[\overline{111}]$
$\pm (111)$	$\pm \frac{1}{3}$	$\pm \frac{2}{3}$	$\pm \frac{1}{3}$	$\pm \frac{1}{3}$
$(111)$	$\pm \frac{2}{3}$	$\pm \frac{1}{3}$	$\pm \frac{1}{3}$	$\pm \frac{1}{3}$
$(022)$	$\pm 1$	$\pm 1$	0	0
$(200)$	$\pm \frac{1}{3}$	$\pm \frac{1}{3}$	$\pm \frac{2}{3}$	$\pm \frac{2}{3}$
$(\bar{3}11)$	0	$\pm 1$	$\pm 1$	$\pm 1$
$(311)$	$\pm 1$	0	$\pm 1$	$\pm 1$

#### 4.3.4 Sample preparation

The deformed samples of Haynes 282 and EHEA were cut parallel to the loading axis using slow speed saw. Later, the cut samples were mounted and grounded using emery sheets followed by diamond and Silica to obtain a mirror finish and strain free surface. These samples are observed in scanning electron microscope to examine for defect microstructures using ECCI and EBSD techniques.

Later, a 0.5 mm strip of sample is sectioned from the deformed sample surface and further reduced the thickness to 100  $\mu\text{m}$  using series of emery sheets. Subsequently, the sample was punched into discs of 3 mm diameter. These disc samples were subjected to electropolishing using twin-jet polishing machine by Struers™ Tenupol-5. Ethanol and perchloric acid in 9:1 volume fraction was used as electrolyte. The equipment was operated at 25 V in  $-30^\circ\text{C}$ .

# CHAPTER 5

---

## Results and Outlook

---

### 5.1 Summary of results

The deformation mechanisms of two classes of materials, namely superalloys and high entropy alloys, are studied using in-situ neutron diffraction technique. The tensile tests are coupled with in-situ neutron diffraction to measure the elastic lattice strains from the considered multi-phase materials. The influence of  $\gamma'$  particle size on the deformation mechanisms of Haynes 282 at room temperature was the first study in this work. This study (paper I in this thesis) has been submitted to Acta Materialia. The latter part was focused on understanding deformation mechanisms of Eutectic high entropy alloy at 77 K, 293 K and 673 K, respectively. This (paper II in this thesis) is in manuscript form. The following sections will discuss briefly about the important merits from both the papers. The reader is requested to refer to the appended paper for further detailed results.

## 5.2 Effect of particle size on load partition of low $\gamma'$ volume fraction superalloy at room temperature deformation

A wrought low  $\gamma'$  volume fraction superalloy, Haynes 282 was provided by GKN Aerospace AB. Two distinct heat treatments were performed to achieve two uni-modal microstructures of  $\gamma'$  particles with fine (20 nm) and coarse (200 nm) in  $\gamma$  matrix. These samples were loaded in tensile mode at room temperature in conjunction with in-situ neutron diffraction. In addition, 2S-elasto-plastic self consistent model (2S-EPSC) was used to compare the evolution of lattice strains and texture of both microstructures from the in-situ neutron diffraction. Later, the deformed samples of two-unimodal microstructures were prepared to analyse using electron microscopy techniques.

The fine structure has higher yield stress than coarser one and both had no significant difference in hardening. The phase specific strain doesn't show significant load partition between  $\gamma$  to  $\gamma'$  for fine  $\gamma'$  structure. The co-deformation of  $\gamma$  and  $\gamma'$  depicts the equal share of plastic and elastic load between them. On contrary, coarse structure has a distinct load transfer from  $\gamma$  to  $\gamma'$  after the yield point. The higher lattice strains in the  $\gamma'$  phase indicates the preferential yielding of  $\gamma$ , resulting in load transfer to elastically deforming  $\gamma'$  particles.

The load partition results from neutron diffraction suggests the fine structure undergoes shearing of particles and coarse  $\gamma'$  particles are surrounded by dense single dislocations often referred as Orowan looping. The orientation specific lattice strains of both microstructure had shown elastic anisotropy. The preferential yielding of (110) / (220) compared to (100) / (200) was observed for fine and coarse structures. The 2S-EPSC simulations were consistent in predicting the evolution of lattice strains for both microstructures. From the peak intensity evolution, both deformed microstructure had shown typical fcc texture with increase in intensity along (200) and (111) and decreasing (220) with strain.

A detailed scanning electron microscopy (SEM) revealed local structural difference in fine and coarse microstructures. Using EBSD, fine structure showed slip bands indicating in-homogeneous deformation, whereas no such bands were noticed in coarse structure. Later, detailed transmission electron microscopy (TEM) was performed exclusively to observe the dislocation activity in both microstructures. The shearing of particles was observed in fine structure by pair of dislocations following pair coupling phenomena indicating the co-deformation of  $\gamma$  and  $\gamma'$ . On the other hand, coarse structure has sparse distribution of dislocations in  $\gamma$ , whereas  $\gamma'$  are circumvented by single dense dislocations due to Orowan looping. This distinct distribution of dislocations in matrix and particle phase confirms the load partition observed

from the neutron diffraction of coarse structure. Finally, the deformation texture from EBSD and 2S-EPSC simulations are found to be consistent for both microstructures.

This work provides critical insights on how load sharing behavior of  $\gamma$  and  $\gamma'$  changes with the size of  $\gamma'$  particles at room temperature deformation in the low volume fraction  $\gamma'$  superalloys.

### 5.3 Effect of deformation temperature on load partition of Eutectic high entropy alloy (EHEA)

Eutectic high entropy with the chemistry of AlCoCrFeNi<sub>2.1</sub> was produced by vacuum arc melting with argon atmosphere to avoid contamination. EHEA has a lamellar microstructure with soft fcc and hard bcc phases enriched with Fe,Co,Cr and Ni,Al, respectively. The as-cast EHEA tensile samples were deformed at 77 K, 300 K and 673 K using in-situ neutron diffraction. Later, the deformed samples were examined using SEM.

The Kurdjumov-Sachs (K-S) relationship between two phases was observed from the initial microstructure characterization. The macroscopic stress-strain response of EHEA varied with the deformation temperature. As expected, increase in strength and decrease in ductility was observed with decreasing temperature. However, the ductility was noticed to be low at all temperatures when compared with the reported literature. Also, the failure strain at 673 K was around 3 % which can prevent the study the plastic deformation of EHEA. The phase specific stress had shown definite load transfer from fcc to bcc, where soft fcc yield and hard bcc deformed elastically at all three temperatures. Further, the orientation specific lattice strains of fcc showed elastic anisotropy. At 77 K and 300 K, the grains along (220) perpendicular to loading direction accommodated large plastic strain without significant work hardening, followed by (200) and (311). Similar trends were clearly observed at room temperature due to large plastic deformation. Further, (200) found to yield early with no work hardening at 673 K in a similar way as in 77 K. However, the other orientations at 673 K had evolved drastically compare to 77 K. Also, (111) had yielded early at 673 K compare to other two temperatures. Overall, fcc had shown a limited work hardening behavior at three temperatures.

The hard bcc phase has shown nearly elastic isotropic behavior at three temperatures. The lattice strains evolution along (110),(211),(220) follow each other and (200) had the largest share of lattice strains among them. The room temperature behavior of (200) was found to be noisy due to very weak (200) peak was obtained probably had a combination of texture and sample orientation on stress rig for diffraction. However, (200) had similar behavior

at 77 K and 673 K with large share of lattice strains, which implies that it has similar trend at room temperature. Furthermore, misorientation analysis was performed using grain reference orientation deviation (GROD) distribution to observe the plastic strain partitioning mechanism between fcc and bcc in three deformed conditions. The GROD distribution of fcc was found to shift to higher values with temperature and noticed to have long tail towards higher angles at room temperature which was absent at 77 K and 673 K. This suggests the limited plastic deformation at 77 K and change in deformation mechanism at 673 K, respectively. On the other hand, bcc GROD distribution had broaden and shifted slightly to higher values with no definite dependency on temperature.

This work provides critical understanding on how the load sharing behavior of soft fcc and hard bcc changes with the temperature in the complex lamellar microstructure of EHEA.

## 5.4 Outlook

The current work was aimed at understanding the load partition between soft and hard phases involving Haynes 282 and EHEA. Haynes was investigated to reveal the load transfer behavior between  $\gamma$  and  $\gamma'$  depending on the size of  $\gamma$  and  $\gamma'$  particle at room temperature. However, the load transfer behavior between matrix and particle phase was unknown at other temperatures with potential industrial applications. Hence, the future work includes in-situ neutron diffraction at cryogenic and elevated temperatures along with EPSC simulations and detailed electron microscopy.

Moving on, EHEA was examined to understand the effect of temperature on load sharing between fcc and bcc at 77 K, 300 K and 673 K using only in-situ neutron diffraction. However, the complementary electron microscopy studies are needed to understand the physical mechanisms involved at the measured temperatures. Also, EPSC models are needed to further understand the deformation mechanisms to predict the lattice strains and texture. Hence, a detailed electron microscopy of EHEA and EPSC model usage will be recommended for future work. Also, the high temperature ( $>673$  K) deformation studies of EHEA were reported in the literature and the load sharing mechanisms are not discussed. Thus, a detailed study on high temperature deformation of EHEA in as-cast condition is planned for future work

---

## Bibliography

---

- [1] Chester T Sims and William C Hagel. *The Superalloys-vital high temperature gas turbine materials for aerospace and industrial power*. John Wiley & Sons, 1972.
- [2] Matthew J Donachie and Stephen J Donachie. *Superalloys: a technical guide*. ASM international, 2002.
- [3] Bhagevatula Satyanarayana Murty, Jien-Wei Yeh, Srinivasa Ranganathan, and PP Bhattacharjee. *High-Entropy Alloys*. Elsevier, 2019.
- [4] Jien Wei Yeh, Swe Kai Chen, Su Jien Lin, Jon Yiew Gan, Tsung Shune Chin, Tao Tsung Shun, Chun Huei Tsau, and Shou Yi Chang. Nanos-structured high-entropy alloys with multiple principal elements: Novel alloy design concepts and outcomes. *Advanced Engineering Materials*, 6(5):299–303, 2004.
- [5] HAYNES 625 alloy, Haynes International. Technical report, 2017.
- [6] L. M. Pike. HAYNES 282 Alloy: A New Wrought Superalloy Designed for Improved Creep Strength and Fabricability. In *Volume 4: Cycle Innovations; Electric Power; Industrial and Cogeneration; Manufacturing Materials and Metallurgy*, page 1031. ASME, 5 2006.
- [7] L.M. Pike. Development of a fabricable gamma-prime ( $\gamma$ ) strengthened superalloy. *Superalloys 2008 (Eleventh International Symposium)*, pages 191–200, 2008.

- [8] Ceena Joseph, Christer Persson, and Magnus Hörnqvist Colliander. Influence of heat treatment on the microstructure and tensile properties of Ni-base superalloy Haynes 282. *Materials Science and Engineering A*, 679:520–530, 2017.
- [9] Magnus Hörnqvist, Ceena Joseph, Christer Persson, Jonathan Weidow, and Haiping Lai. Dynamic strain aging in Haynes 282 superalloy. *MATEC Web of Conferences*, 14:16002, 8 2014.
- [10] R. Brommesson, M. Ekh, and M. Hörnqvist. Correlation between crack length and load drop for low-cycle fatigue crack growth in Ti-6242. *International Journal of Fatigue*, 81:1–9, 12 2015.
- [11] B. Cantor, I. T H Chang, P. Knight, and A. J B Vincent. Microstructural development in equiatomic multicomponent alloys. *Materials Science and Engineering A*, 375-377(1-2 SPEC. ISS.):213–218, 2004.
- [12] F. Zhang, C. Zhang, S. L. Chen, J. Zhu, W. S. Cao, and U. R. Kattner. An understanding of high entropy alloys from phase diagram calculations. *Calphad: Computer Coupling of Phase Diagrams and Thermochemistry*, 45:1–10, 6 2014.
- [13] Zhiming Li, Konda Gokuldoss Pradeep, Yun Deng, Dierk Raabe, and Cemal Cem Tasan. Metastable high-entropy dual-phase alloys overcome the strength-ductility trade-off. *Nature*, 534(7606):227–230, 6 2016.
- [14] J Y He, H Wang, H L Huang, X D Xu, M W Chen, Y Wu, X J Liu, T G Nieh, K An, and Z P Lu. A precipitation-hardened high-entropy alloy with outstanding tensile properties. *Acta Materialia*, 102:187–196, 2016.
- [15] J Y He, H Wang, Y Wu, X J Liu, H H Mao, T G Nieh, and Z P Lu. Precipitation behavior and its effects on tensile properties of FeCoNiCr high-entropy alloys. *Intermetallics*, 79:41–52, 2016.
- [16] Yiping Lu, Yong Dong, Sheng Guo, Li Jiang, Huijun Kang, Tongmin Wang, Bin Wen, Zhijun Wang, Jinchuan Jie, Zhiqiang Cao, Haihui Ruan, and Tingju Li. A promising new class of high-temperature alloys: Eutectic high-entropy alloys. *Scientific Reports*, 4(1):6200, 5 2014.
- [17] Yiping Lu, Xuzhou Gao, Li Jiang, Zongning Chen, Tongmin Wang, Jinchuan Jie, Huijun Kang, Yubo Zhang, Sheng Guo, Haihui Ruan, Yonghao Zhao, Zhiqiang Cao, and Tingju Li. Directly cast bulk eutectic and near-eutectic high entropy alloys with balanced strength and ductility in a wide temperature range. *Acta Materialia*, 124:143–150, 2 2017.
- [18] M. F. Ashby. A first report on deformation-mechanism maps. *Acta Metallurgica*, 20(7):887–897, 7 1972.

- [19] Terence G. Langdon and Farghalli A. Mohamed. A simple method of constructing an Ashby-type deformation mechanism map. *Journal of Materials Science*, 13(6):1282–1290, 6 1978.
- [20] Derek Hull and David J Bacon. *Introduction to dislocations*. Butterworth-Heinemann, 2001.
- [21] Hans Cosrad. Effect of temperature on yield and flow stress of B.C.C. metals. *Philosophical Magazine*, 5(55):745–751, 7 1960.
- [22] D Brunner and V Glebovsky. Plastic properties of high-purity W single crystals. *Materials Letters*, 42(5):290–296, 2 2000.
- [23] A Lawley and H L Gaigher. Deformation structures in zone-melted molybdenum. *Philosophical Magazine*, 10(103):15–33, 1964.
- [24] U. F. Kocks. The relation between polycrystal deformation and single-crystal deformation. *Metallurgical and Materials Transactions*, 1(5):1121–1143, 5 1970.
- [25] C R Weinberger, B L Boyce, and C C Battaile. Slip planes in bcc transition metals. *International Materials Reviews*, 58(5):296–314, 6 2013.
- [26] A Seeger. The Temperature and Strain-Rate Dependence of the Flow Stress of Body-Centred Cubic Metals: A Theory Based on Kink-Kink Interactions. *Zeitschrift fur Metallkunde*, 72(6):369–380, 1981.
- [27] M Z Butt. Kinetics of flow stress in crystals with high intrinsic lattice friction. *Philosophical Magazine*, 87(24):3595–3614, 2007.
- [28] M Duesbery, S, and V Vitek. Plastic anisotropy in bcc transition metals. *Acta Materialia*, 46(5):1481–1492, 1998.
- [29] K Ito and V Vitek. Atomistic study of non-Schmid effects in the plastic yielding of bcc metals. *Philosophical Magazine A*, 81(5):1387–1407, 2001.
- [30] Roger C. Reed. 2 The physical metallurgy of nickel and its alloys. *Superalloys- Fundamentals and Applications*, pages 33–120, 2006.
- [31] N. S. Stoloff. Physical and mechanical metallurgy of Ni3Al and its alloys. *International Materials Reviews*, 34(1):153–184, 1 1989.
- [32] W Huther and B Reppich. Interaction of dislocations with coherent, stress-free ordered particles. *Zeitschrift Fur Metallkunde*, 69:628–634, 1978.
- [33] H. Gleiter and E. Hornbogen. Theorie der Wechselwirkung von Versetzungen mit kohärenten geordneten Zonen (I). *physica status solidi (b)*, 12(1):235–250, 1 1965.

- [34] H. Gleiter and E. Hornbogen. Beobachtung der Wechselwirkung von Versetzungen mit kohärenten geordneten Zonen (II). *physica status solidi (b)*, 12(1):251–264, 1 1965.
- [35] D. Raynor and J. M. Silcock. Strengthening Mechanisms in  $\gamma$  Precipitating Alloys. *Metal Science Journal*, 4(1):121–130, 1 2014.
- [36] E. J. Pickering and N. G. Jones. High-entropy alloys: a critical assessment of their founding principles and future prospects. *International Materials Reviews*, 61(3):183–202, 2016.
- [37] Jien Wei Yeh. Alloy design strategies and future trends in high-entropy alloys. *JOM*, 65(12):1759–1771, 12 2013.
- [38] Jien-Wei Yeh and Su-Jien Lin. Breakthrough applications of high-entropy materials. *Journal of Materials Research*, 33(19):3129–3137, 10 2018.
- [39] Louis J. Santodonato, Yang Zhang, Mikhail Feygenson, Chad M. Parish, Michael C. Gao, Richard J.K. Weber, Joerg C. Neuefeind, Zhi Tang, and Peter K. Liaw. Deviation from high-entropy configurations in the atomic distributions of a multi-principal-element alloy. *Nature Communications*, 6:1–13, 2015.
- [40] Qing-Jie Li, Howard Sheng, and Evan Ma. Strengthening in multi-principal element alloys with local-chemical-order roughened dislocation pathways. *Nature Communications*, 10(1):3563, 2019.
- [41] Y. Wu, W. H. Liu, X. L. Wang, D. Ma, A. D. Stoica, T. G. Nieh, Z. B. He, and Z. P. Lu. In-situ neutron diffraction study of deformation behavior of a multi-component high-entropy alloy. *Applied Physics Letters*, 104(5), 2014.
- [42] Tao Yang, Yilu Zhao, Weihong Liu, Jijung Kai, and Chaintsuan Liu. L12-strengthened high-entropy alloys for advanced structural applications, 10 2018.
- [43] Yifeng Liao and Ian Baker. Microstructure and room-temperature mechanical properties of Fe<sub>30</sub>Ni<sub>20</sub>Mn<sub>35</sub>Al<sub>15</sub>. *Materials Characterization*, 59(11):1546–1549, 11 2008.
- [44] Michael Preuss, João Quinta da Fonseca, Benedict Grant, Elisabeth Knoche, Richard Moat, and Mark Daymond. The effect of  $\gamma'$  particle size on the deformation mechanism in an advanced polycrystalline nickel-base superalloy. *Superalloys 2008: 11th International Symposium on Superalloys*, (010):405–414, 2008.
- [45] Benedict M B Grant, Elisabeth M. Francis, Joao Quinta Da Fonseca, Mark R. Daymond, and Michael Preuss. Deformation behaviour of an advanced nickel-based superalloy studied by neutron diffraction and electron microscopy. *Acta Materialia*, 60:6829–6841, 11 2012.

- [46] E. M. Francis, B. M B Grant, J. Quinta Da Fonseca, P. J. Phillips, M. J. Mills, M. R. Daymond, and M. Preuss. High-temperature deformation mechanisms in a polycrystalline nickel-base superalloy studied by neutron diffraction and electron microscopy. *Acta Materialia*, 74:18–29, 2014.
- [47] Jae Wung Bae, Jae Bok Seol, Jongun Moon, Seok Su Sohn, Min Ji Jang, Ho Yong Um, Byeong Joo Lee, and Hyoung Seop Kim. Exceptional phase-transformation strengthening of ferrous medium-entropy alloys at cryogenic temperatures. *Acta Materialia*, 161:388–399, 12 2018.
- [48] L. R. Owen, E. J. Pickering, H. Y. Playford, H. J. Stone, M. G. Tucker, and N. G. Jones. An assessment of the lattice strain in the CrMnFeCoNi high-entropy alloy. *Acta Materialia*, 122:11–18, 2017.
- [49] Wanchuck Woo, E. Wen Huang, Jien Wei Yeh, Hahn Choo, Chi Lee, and Shan Yi Tu. In-situ neutron diffraction studies on high-temperature deformation behavior in a CoCrFeMnNi high entropy alloy. *Intermetallics*, 62:1–6, 2015.
- [50] Zhiqiang Fu, Lin Jiang, Jenna L Wardini, Benjamin E MacDonald, Haiming Wen, Wei Xiong, Dalong Zhang, Yizhang Zhou, Timothy J Rupert, Weiping Chen, and Enrique J Lavernia. A high-entropy alloy with hierarchical nanoprecipitates and ultrahigh strength. *Science Advances*, 4(10):1–9, 2018.
- [51] Yiqiang Wang, Bin Liu, Kun Yan, Minshi Wang, Saurabh Kabra, Yu-Lung Chiu, David Dye, Peter D. Lee, Yong Liu, and Biao Cai. Probing deformation mechanisms of a FeCoCrNi high-entropy alloy at 293 and 77 K using in situ neutron diffraction. *Acta Materialia*, 5 2018.
- [52] F. Otto, Y. Yang, H. Bei, and E. P. George. Relative effects of enthalpy and entropy on the phase stability of equiatomic high-entropy alloys. *Acta Materialia*, 61(7):2628–2638, 4 2013.
- [53] Sathiyamoorthi Praveen and Hyoung Seop Kim. High-Entropy Alloys: Potential Candidates for High-Temperature Applications – An Overview. *Advanced Engineering Materials*, 20(1):1–22, 2018.
- [54] K. Y. Tsai, M. H. Tsai, and J. W. Yeh. Sluggish diffusion in Co-Cr-Fe-Mn-Ni high-entropy alloys. *Acta Materialia*, 61(13):4887–4897, 8 2013.
- [55] Tilak Bhattacharjee, Ruixiao Zheng, Yan Chong, Saad Sheikh, Sheng Guo, Ian Thomas Clark, Toshiro Okawa, Irfan Samad Wani, Pinaki Prasad Bhattacharjee, Akinobu Shibata, and Nobuhiro Tsuji. Effect of low temperature on tensile properties of AlCoCrFeNi 2.1 eutectic high entropy alloy. *Materials Chemistry and Physics*, pages 1–6, 2017.

- [56] Xuzhou Gao, Yiping Lu, Bo Zhang, Ningning Liang, Guanzhong Wu, Gang Sha, Jizi Liu, and Yonghao Zhao. Microstructural origins of high strength and high ductility in an AlCoCrFeNi<sub>2.1</sub> eutectic high-entropy alloy. *Acta Materialia*, 141:59–66, 2017.
- [57] Yaoli Zhang, Xinguang Wang, Jinguo Li, Yaqi Huang, Yiping Lu, and Xiaofeng Sun. Deformation mechanism during high-temperature tensile test in an eutectic high-entropy alloy AlCoCrFeNi<sub>2.1</sub>. *Materials Science and Engineering A*, 724:148–155, 5 2018.
- [58] I. S. Wani, T. Bhattacharjee, S. Sheikh, Y. P. Lu, S. Chatterjee, P. P. Bhattacharjee, S. Guo, and N. Tsuji. Ultrafine-Grained AlCoCrFeNi<sub>2.1</sub> Eutectic High-Entropy Alloy. *Materials Research Letters*, 4(3):174–179, 2016.
- [59] T. Bhattacharjee, I. S. Wani, S. Sheikh, I. T. Clark, T. Okawa, S. Guo, P. P. Bhattacharjee, and N. Tsuji. Simultaneous Strength-Ductility Enhancement of a Nano-Lamellar AlCoCrFeNi<sub>2.1</sub> Eutectic High Entropy Alloy by Cryo-Rolling and Annealing. *Scientific Reports*, 8(1):3276, 12 2018.
- [60] A. Patel, I. Wani, S.R. Reddy, S. Narayanaswamy, A. Lozinko, R. Saha, S. Guo, and P.P. Bhattacharjee. Strain-path controlled microstructure, texture and hardness evolution in cryo-deformed AlCoCrFeNi<sub>2.1</sub> eutectic high entropy alloy. *Intermetallics*, 97:12–21, 6 2018.
- [61] Peijian Shi, Weili Ren, Tianxiang Zheng, Zhongming Ren, Xueling Hou, Jianchao Peng, Pengfei Hu, Yanfei Gao, Yunbo Zhong, and Peter K. Liaw. Enhanced strength–ductility synergy in ultrafine-grained eutectic high-entropy alloys by inheriting microstructural lamellae. *Nature Communications*, 10(1):489, 12 2019.
- [62] S.R. Reddy, S. Yoshida, T. Bhattacharjee, N. Sake, A. Lozinko, S. Guo, P.P. Bhattacharjee, and N. Tsuji. Nanostructuring with Structural-Compositional Dual Heterogeneities Enhances Strength-Ductility Synergy in Eutectic High Entropy Alloy. *Scientific Reports*, 9(1):11505, 12 2019.
- [63] William Henry Bragg and William Lawrence Bragg. *X-rays and Crystal Structure*. G. Bell and sons, Limited, 1918.
- [64] J. R. Santisteban, M. R. Daymond, J. A. James, and L. Edwards. ENGIN-X: A third-generation neutron strain scanner. *Journal of Applied Crystallography*, 39:812–825, 2006.
- [65] Allison M Beese, Zhuqing Wang, Alexandru D Stoica, and Dong Ma. Absence of dynamic strain aging in an additively manufactured nickel-base superalloy. *Nature communications*, 9(1):2083, 2018.

- [66] Brian H. Toby, Robert B. Von Dreele, and IUCr.  $\mu$ iGSAS-II/i $\mu$ : the genesis of a modern open-source all purpose crystallography software package. *Journal of Applied Crystallography*, 46(2):544–549, 4 2013.
- [67] R. Hill. Continuum micro-mechanics of elastoplastic polycrystals. *Journal of the Mechanics and Physics of Solids*, 13:89–101, 4 1965.
- [68] J. W. Hutchinson. Elastic-Plastic Behaviour of Polycrystalline Metals and Composites. *Proceedings of the Royal Society A: Mathematical, Physical and Engineering Sciences*, 319:247–272, 10 1970.
- [69] P A Turner and C N Tomé. A Study of Residual Stresses in \protectZircaloy-2 with Rod Texture. *Acta Materialia*, 42(12):4043–4055, 1994.
- [70] R. A. Lebensohn and G. R. Canova. A self-consistent approach for modelling texture development of two-phase polycrystals: Application to titanium alloys. *Acta Materialia*, 45(9):3687–3694, 9 1997.
- [71] D. Dye, H. J. Stone, and R. C. Reed. A two phase elastic-plastic self-consistent model for the accumulation of microstrains in Waspaloy. *Acta Materialia*, 49:1271–1283, 2001.
- [72] Hongjia Li, Magnus Ekh, Magnus Hörnqvist Colliander, and Fredrik Larsson. Accounting for lattice coherency in a two-phase elastic-plastic self-consistent model for nickel-based superalloys. *International Journal of Plasticity*, 110:2478–271, 2018.
- [73] U Fred Kocks, Carlos Norberto Tomé, H-R Wenk, and Armand J Beaudoin. *Texture And Anisotropy: Preferred Orientations in Polycrystals and Their Effect on Materials Properties*. Cambridge University Press, 2000.
- [74] C. N. Tomé, P. J. Maudlin, R. A. Lebensohn, and G. C. Kaschner. Mechanical response of zirconium - I. Derivation of a polycrystal constitutive law and finite element analysis. *Acta Materialia*, 49:3085–3096, 9 2001.
- [75] David C Joy, Dale E Newbury, and David L Davidson. Electron channeling patterns in the scanning electron microscope. *Journal of Applied Physics*, 53:R81–R122, 1982.
- [76] Olaf Engler and Gunter Gottstein. New approach in texture research: local orientation determination with EBSP. *Steel Research*, 63(9):413–418, 9 1992.
- [77] Stuart I. Wright, Matthew M. Nowell, and David P. Field. A review of strain analysis using electron backscatter diffraction, 5 2011.
- [78] David B Williams and C Barry Carter. The transmission electron microscope. pages 3–17, 1996.